Check for updates

RESEARCH ARTICLE

NANO · MICRO small
www.small-journal.com

Electronic Structure Engineering of Pt–Ni Alloy NPs by Coupling of Gold Single Atoms on N-Doped Carbon for Highly Efficient Oxygen Reduction Reaction and Hydrogen Evolution Reaction

*Thanh Duc Le, Dong-Seog Kim, Tuong Van Tran, Bharagav Urupalli, Gi-Seung Shin, Geun-Jae Oh, and Yeon-Tae Yu**

Improving the catalytic activity and durability of platinum-based alloy catalysts remains a formidable challenge in the context of renewable energy electrolysis applications. Herein, a facile and rapid photochemical deposition strategy for the synthesis of gold single atoms (Au SAs) anchored on N-doped carbon is presented. These Au SAs serve as a charge redistribution support for Pt–Ni alloy nanoparticles ($PtNi_{NPs}/Au_{SA}$-NDC), creating an extended electron-donating interface with Pt–Ni alloy sites. Consequently, the $PtNi_{NPs}/Au_{SA}$-NDC hybrid catalyst manifests exceptional catalytic performance and durability in both the oxygen reduction reaction (ORR) and hydrogen evolution reaction (HER) under acidic conditions. Specifically, in ORR, it exhibits a half-wave potential (0.92 V vs RHE), with a mass activity 20.4 times superior to Pt/C at 0.9 V. In HER, $PtNi_{NPs}/Au_{SA}$-NDC demonstrates a notably reduced overpotential of 19.1 mV vs RHE at 10 mA cm^{-2} and a mass activity 38 times higher than Pt/C (at 0.25 mV). Furthermore, this hybrid catalyst displays outstanding durability, with only an 8.0 mV decay observed for ORR and a 6.9 mV decay for HER after 10 000 cycles. Theoretical calculations provide insight into the mechanism, demonstrating that isolated Au sites effectively modulate the electronic structure of Pt–Ni alloy sites, facilitating intermediate adsorption and enhancing reaction kinetics.

1. Introduction

The ever-increasing global consumption of fossil fuels has emerged as a paramount concern in the context of climate change, with an ambitious global target set to achieve carbon neutrality by 2050.[1] In response to this imperative, two key green and renewable energy technologies have garnered significant attention: hydrogen production through water splitting and electricity generation using fuel cells. These technologies rely on the potential to efficiently produce hydrogen and convert the chemical energy stored within hydrogen molecules into electricity. The efficacy of energy conversion from chemical to electrical forms in both fuel cells and electrocatalytic water-splitting cells is fundamentally governed by two key electrochemical reactions: the hydrogen evolution reaction (HER) and the oxygen reduction reaction (ORR).[2] It is noteworthy to mention that the predominant proportion of electrocatalysts employed in the ORR and HER processes are based on the noble metal platinum (Pt). Remarkably, Pt can contribute significantly to the overall cost, accounting for as much as 30–40% of the total device expenses.[3] Moreover, the intricate electron transfer mechanisms and inherently sluggish reaction kinetics pose formidable challenges that hinder the widespread utilization of Pt in commercial applications.[4,5] Thus, developing cost-effective, stable, and highly active Pt-based electrocatalysts is essential to reduce reliance on Pt and advance sustainable energy solutions.

In order to improve the electrocatalytic performance of Pt, researchers have made extensive efforts to synthesize Pt-based alloy, expose high-index crystal faces, and manufacture core–shell nanostructures.[6,7] It is noteworthy to mention that the design of Pt-based alloy with transition metals (Pt–M, M = Co, Ni, Fe, Cu, etc.) has demonstrated a feasible approach to promote the utilization efficiency of Pt catalyst by downshifting the position of the d-band center of Pt sites, thus enhancing the catalytic activity of Pt.[8–12] However, Pt–M alloy electrocatalysts typically experience a significant decrease in activity under harsh conditions due to the leaching of transition metals from alloy nanoparticles.[13,14] The stability of Pt–M alloy catalysts can be improved to some

T. D. Le, D.-S. Kim, T. V. Tran, B. Urupalli, G.-S. Shin, G.-J. Oh, Y.-T. Yu
Division of Advanced Materials Engineering
Research Center for Advanced Materials Development
Jeonbuk National University
Jeonju 54896, South Korea
E-mail: yeontae@jbnu.ac.kr
The ORCID identification number(s) for the author(s) of this article can be found under https://doi.org/10.1002/smll.202311971

© 2024 The Authors. Small published by Wiley-VCH GmbH. This is an open access article under the terms of the Creative Commons Attribution-NonCommercial License, which permits use, distribution and reproduction in any medium, provided the original work is properly cited and is not used for commercial purposes.

DOI: 10.1002/smll.202311971

extent through a phase transition from disordered solid solution structures to ordered intermetallic phases or carbon layers coating the surface of Pt–M alloy NPs.[15–19] Unfortunately, this generally works at the cost of reduced activity because high-temperature treatments in the phase conversion result in crystal growth, or the outer dense carbon layers can hinder the reactant access to the active sites of Pt–M alloy catalyst.[17] Therefore, the present state of Pt-based alloy electrocatalysts falls short in terms of enabling the design of industrially scalable electrochemical catalysts, and their stability needs to be further improved.

Gold (Au) is one of the most intriguing examples in the field of nanocatalysis, demonstrating the transformation from its catalytically inert bulk state to highly active forms of clusters and NPs. Numerous studies have shown that tiny Au clusters exhibit remarkable catalytic activity and selectivity, which are strongly size-dependent.[20,21] This is particularly evident in oxidation reactions involving molecular oxygen, owing to its capability to activate the O—O bonds,[22–24] as well as reactions involving hydrogen bonding activation and hydrogen dissociation.[25–27] Meanwhile, since the discovery of single-atom (SA) catalysts, the world of highly efficient electrocatalysts has expanded to a vast domain. From the nanoparticles to nanoclusters or even SA catalysts, the intrinsic activity of their catalytic active sites can be improved with the size reduction due to the lower coordination environment of the metal center, quantum size effects, and strong metal-support interactions.[28,29] More importantly, by combining the foreign metallic SA sites such as Au, Fe, Co, and Ni SA with Pt-based NP catalysts, the synergistic effects can be presented in improving the catalytic activity and stability.[30–33] For instance, Liu et al.[34] introduced an ORR electrocatalyst comprising core–shell Pt alloy nanoparticles deposited on an SA Fe support. This distinctive microstructure, along with the interaction between the Pt alloy and SA Fe sites, significantly enhanced the ORR performance. During the past decades, several strategies for atomically dispersing metal sites on catalyst supports have emerged; these include the solution chemical method,[35] high-temperature pyrolysis,[36] atomic layer deposition,[37] and ball-milling method.[38] However, it is noteworthy that these approaches typically entail elevated energy consumption and considerable time expenditures. The photochemical deposition method is regarded as a cost-effective, room-temperature technique for the preparation of single-atom (SA) catalysts. Under the influence of photogenerated electrons, it is possible to modulate the valence state of the active centers.[39–41] Recently, Wu et al. reported an iced-photochemical reduction to fabricate atomic Pt catalysts via ultraviolet irradiation reduction of frozen chloroplatinic acid aqueous solution for electrochemical HER.[42]

In this study, we design $PtNi_{NPs}/Au_{SA}$-NDC (N-doped carbon) nanocomposite with the aim of further improving the catalytic activity and durability of Pt–Ni alloy NPs catalysts and present a room-temperature photochemical deposition approach to efficiently load Au SAs onto NDC supported Pt–Ni alloy NPs. Here, Au SAs are tightly clamped between Pt–Ni alloy NPs and N-doped carbon, serving as a charge redistribution support for Pt–Ni alloy NPs. The hybrid structure of Pt–Ni alloy NPs coupled with Au SAs enables efficient electron transfer between these individual sites, realizing superior bifunctional catalytic activity and enhanced durability for ORR and HER. The robust coordination structure of Au-N_x SAs bonding is meticulously investigated through aberration-corrected high-angle annular dark-field scanning transmission electron microscopy (HAADF-STEM) and X-ray photoelectron spectroscopy (XPS) analysis. Finally, the mechanism for the enhancement in the catalytic performance of the synthesized $PtNi_{NPs}/Au_{SA}$-NDC catalyst is discussed based on density functional theory (DFT) calculations.

2. Results and Discussion

2.1. Structural Characterizations

We developed a two-step method that combines solvothermal and photochemical deposition to synthesize the $PtNi_{NPs}/Au_{SA}$-NDC hybrid catalyst. Initially, octahedral Pt–Ni alloy NPs were synthesized using the solvothermal method and subsequently loaded uniformly on N-doped carbon (NDC) derived from ZIF-8 (BET of 1638.5 $m^2\ g^{-1}$ in Figure S1, Supporting Information). A comprehensive illustration of the stepwise preparation of the $PtNi_{NPs}/Au_{SA}$-NDC hybrid catalyst can be found in **Figure 1**. The X-ray diffraction (XRD) pattern, as shown in **Figure 2a**, indicates the complete carbonization of ZIF-8 to form NDC, exhibiting an absence of characteristic metallic peaks of Pt and Ni. The FE-SEM and HAADF-STEM images revealed that there are no metal species within the matrix of dodecahedrons NDC (Figure S2 and S3, Supporting Information). Subsequently, the Pt–Ni alloy NPs loaded onto NDC (Figure S4 and S5, Supporting Information) were then immersed in a solution containing an appropriate quantity of $HAuCl_4$ and exposed to visible light for 5 min. Due to its physical admixture with the $HAuCl_4$ solution, NDC effectively adsorbs Au^{3+} cations from the solution. This exceptional adsorption capability stems from NDC's remarkably high specific surface area (1131.6 $m^2\ g^{-1}$) and the presence of abundant micropores (average pore diameter of 3.9 nm), which are corroborated by nitrogen adsorption–desorption measurements (Figure S6a, Supporting Information). Xenon light was employed to irradiate the aforementioned mixture, as a result, Au^{3+} cations were reduced by photogenerated electrons to Au SAs.[43] In a comparative experiment, we prepared the Au_{SA}-NDC catalyst using the same method without loading Pt–Ni alloy nanoparticles. As depicted in Figure S7 (Supporting Information), the post-irradiation morphology of the Au_{SA}-NDC catalyst was similar to the pure NDC except there are a few Au nanoclusters or NPs on the carbon surface. However, numerous bright dots (highlighted by red circles) are also found on the NDC surface. This suggests that the reduced Au species may mostly exist at atomically small sizes.

The XRD patterns were adopted to determine the crystalline phase of $PtNi_{NPs}/Au_{SA}$-NDC before and after photochemical deposition of Au SAs (Figure 2a). The diffraction peaks (2θ) located at 40.5°, 47.3°, and 69.3°, corresponding to (111), (200), and (220) crystallographic planes, respectively. The peak positions of $PtNi_{NPs}/Au_{SA}$-NDC and $PtNi_{NPs}$/NDC shift slightly toward higher 2θ angles compared to pure Pt, which is in alignment with Pt–Ni (111) alloy facet (PDF#65-9445).[44] Additionally, in accordance with Bragg's law, the calculated d-spacing is found to be 0.22 nm, which is perfectly aligned with the (111) plane of the alloy nanoparticles. Furthermore, Figure 2b shows the Pt–Ni (111) peak of $PtNi_{NPs}/Au_{SA}$-NDC and $PtNi_{NPs}$/NDC in the range of 36°–44°. There is no peak shift is observed,

© 2024 The Authors. Small published by Wiley-VCH GmbH

16136829, 2024, 34, Downloaded from https://onlinelibrary.wiley.com/doi/10.1002/smll.202311971 by Jeonbuk National University, Wiley Online Library on [18/10/2026]. See the Terms and Conditions (https://onlinelibrary.wiley.com/terms-and-conditions) on Wiley Online Library for rules of use; OA articles are governed by the applicable Creative Commons License

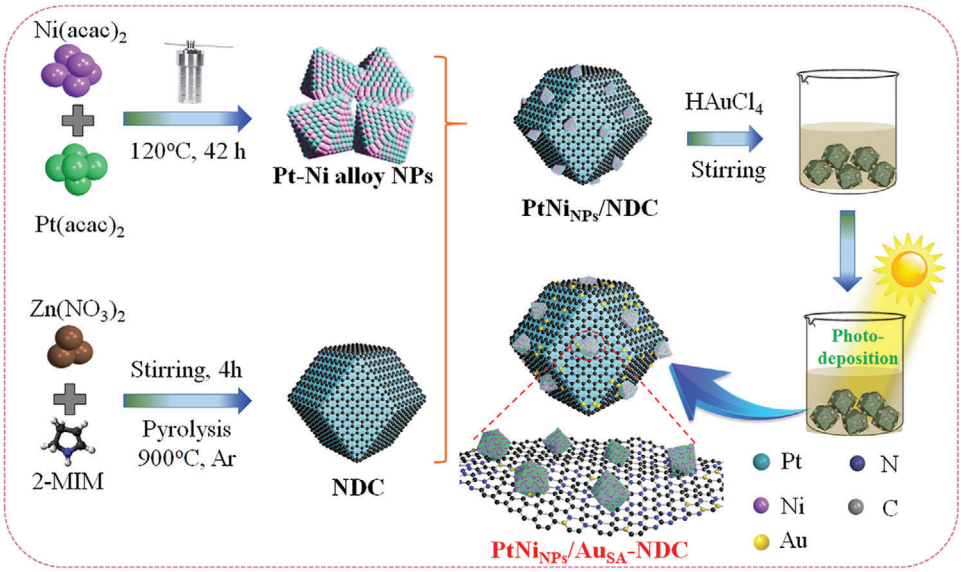


Figure 1. Schematic illustration of the synthesis process of the $PtNi_{NPs}/Au_{SA}$-NDC hybrid catalysts.

indicating that there is no substitution of Au atoms with Pt or Ni in Pt–Ni alloy NPs after the photochemical deposition process. In particular, for Au_{SA}-NDC, a distinctive minor diffraction peak located at 38.2° is consistent with the (111) crystal facet of Au metal (PDF#00-004-0784).[45] In addition, the Au (111) peak of $PtNi_{NPs}/Au_{SA}$-NDC is sis significantly decreasing compared with Au_{SA}-NDC, suggesting that the existence of Pt–Ni alloy NPs seems to inhibit the formation of Au crystals. As observed in Figure S6 (Supporting Information), the BET-specific surface area decreases from 1131.6 $m^2\ g^{-1}$ for the NDC support to 935.1 $m^2\ g^{-1}$ after loading Pt–Ni alloy NPs, suggesting that the existence of Pt–Ni alloy NPs potentially hindering the anchoring

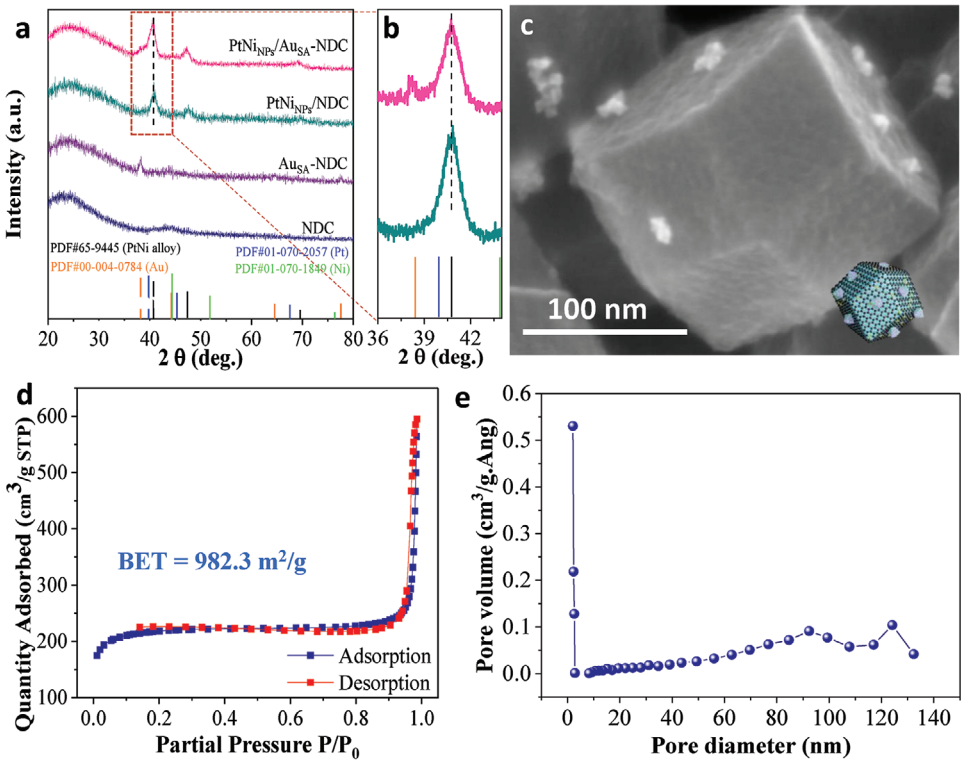


Figure 2. a, b) X-ray Diffraction patterns of NDC, Au_{SA}-NDC, $PtNi_{NPs}$/NDC and $PtNi_{NPs}/Au_{SA}$-NDC. c) FE-SEM, d) N_2 sorption isotherm profile, and e) the corresponding pore size distribution of the as-prepared $PtNi_{NPs}/Au_{SA}$-NDC catalysts.

© 2024 The Authors. Small published by Wiley-VCH GmbH

16136829, 2024, 34, Downloaded from https://onlinelibrary.wiley.com/doi/10.1002/smll.202311971 by Jeonbuk National University, Wiley Online Library on [18/10/2026]. See the Terms and Conditions (https://onlinelibrary.wiley.com/terms-and-conditions) on Wiley Online Library for rules of use; OA articles are governed by the applicable Creative Commons License

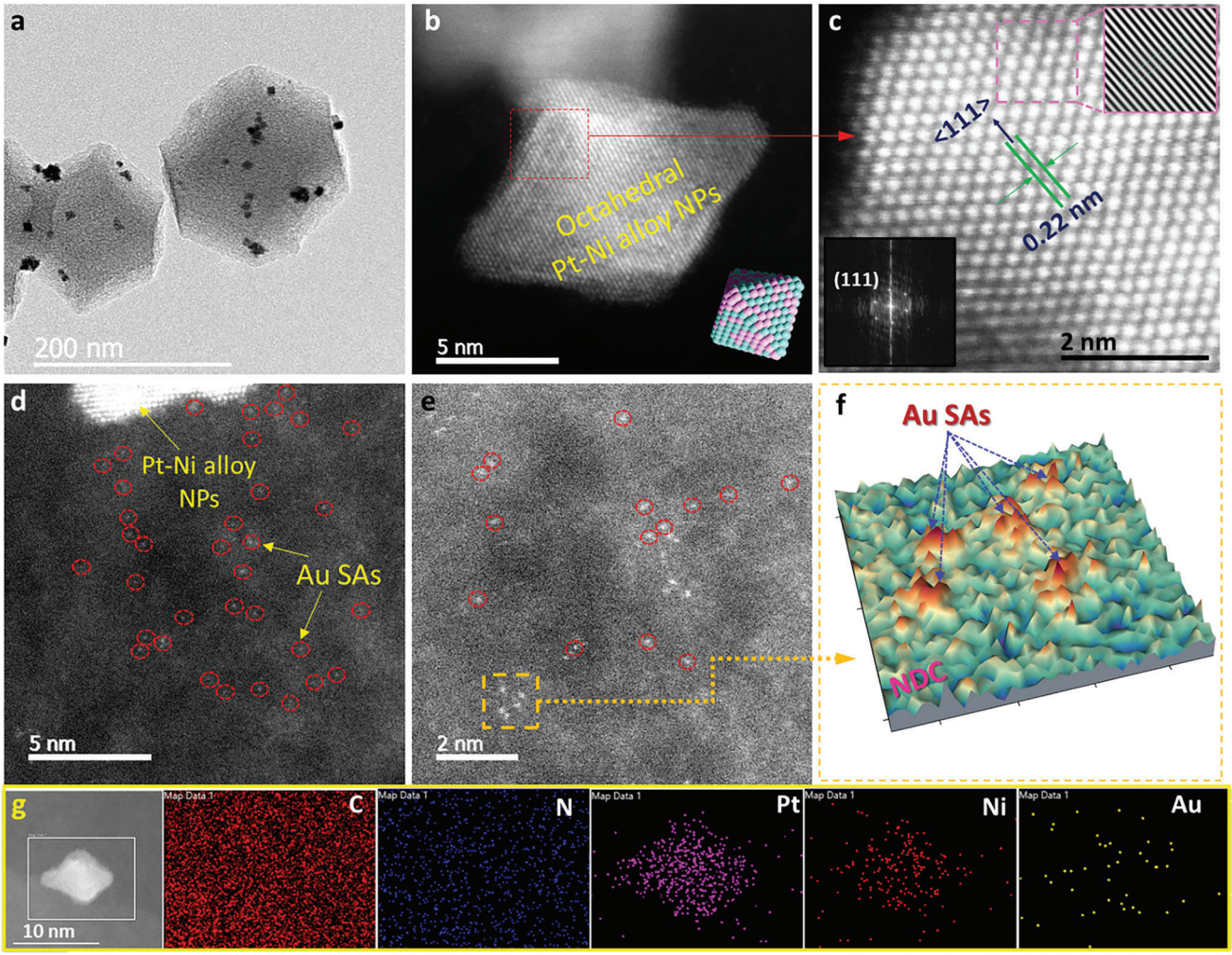


Figure 3. a) TEM image of $PtNi_{NPs}/Au_{SA}$-NDC, b) HAADF-STEM image of an individual Pt–Ni alloy NP along with its crystalline features at the c) selected area. d, e) The HAADF-STEM image $PtNi_{NPs}/Au_{SA}$-NDC at an area with and without Pt–Ni alloy NPs, f) the 3D map intensity profile of the selected atoms in marked with an orange box in (e). g) The EDX color mapping of C (red), N (blue), Pt (pink), Ni (orange), and Au (yellow).

points of N-doped carbon for the formation of Au SAs. This phenomenon aligns with the ICP-MS results, indicating that the Au metal loading amount in PtNiNPs/AuSA-NDC and AuSA-NDC is 0.41 and 0.54 wt.%, respectively (Table S1, Supporting Information).

This observation strongly supports the formation of Au SAs after the photochemical deposition process. To determine the optimal Au loading on NDC (Figure S8a, Supporting Information), we conducted linear sweep voltammetry in an O_2-saturated 0.1 M $HClO_4$ (Figure S8b, Supporting Information). Various $PtNi_{NPs}/Au_{SA}$-NDC catalysts with different Au loading amounts were prepared and tested. Notably, the $PtNi_{NPs}/Au_{SA}$-NDC with 0.5 wt.% Au loading exhibits the highest haft-wave potential. Further insight into the morphology of $PtNi_{NPs}/Au_{SA}$-NDC hybrid catalysts is provided by FE-SEM images (Figure 2c), revealing that they maintain the dodecahedral shape observed in blank NDC. On the other hand, Brunauer–Emmett–Teller (BET) analysis was also employed to determine the BET surface area and pore distribution using N_2 adsorption/desorption isotherms as shown in Figure 2d,e. The BET surface area of $PtNi_{NPs}/Au_{SA}$-NDC is 982.3 $m^2\ g^{-1}$ and pore size distribution data indicates that the synthesis material possesses a combination of micropores from ZIF8-derived porous carbon and macropores from the pores between $PtNi_{NPs}$ particles. The Raman spectroscopy was used to verify the defect structure of the as-synthesized catalysts (Figure S9, Supporting Information). Two sharp characteristic peaks, the D band at 1350 cm^{-1} and the G band at 1580 cm^{-1}, were assigned to the lattice defects and sp^2-hybridized carbon, respectively.[8] The I_D/I_G ratio was calculated from the D band and G band peak area. The I_D/I_G ratio for $PtNi_{NPs}/Au_{SA}$-NDC (1.12) was higher than that of Au_{SA}-NDC (1.07), $PtNi_{NPs}$/NDC (0.95) and NDC (0.97), indicating that anchoring Au SAs resulted in a higher number of defects (I_D/I_G).[46,47]

To further corroborate the formation of Pt–Ni alloy NPs and Au SAs, atomic-resolution aberration-corrected scanning transmission microscopy (STEM) was employed for the synthesized $PtNi_{NPs}/Au_{SA}$-NDC. **Figure 3a** presents a typical TEM image of our synthesized hybrid catalyst, showing the uniform size

© 2024 The Authors. Small published by Wiley-VCH GmbH

16136829, 2024, 34, Downloaded from https://onlinelibrary.wiley.com/doi/10.1002/smll.202311971 by Jeonbuk National University, Wiley Online Library on [18/10/2026]. See the Terms and Conditions (https://onlinelibrary.wiley.com/terms-and-conditions) on Wiley Online Library for rules of use; OA articles are governed by the applicable Creative Commons License

distribution of Pt–Ni alloy NPs with an average particle size of 8.73 nm (as illustrated in Figure S10, Supporting Information). As evident in Figure 3b,c, the Pt–Ni alloy nanocrystals exhibit a characteristic octahedral structure, which is a well-known feature of precious metal alloy nanostructures renowned for their high ORR activity.[45] In-depth analysis using high-resolution HAADF-STEM reveals a d-spacing of 2.2 Å corresponding to the lattice spacing of (111) crystallographic planes of Pt–Ni alloy NPs. This observation corroborates the results of X-ray diffraction (XRD) and selected area electron diffraction (SAED). Significantly, the Pt–Ni alloy NPs in the $PtNi_{NPs}/Au_{SA}$-NDC material maintain their original d-spacing and octahedral shape even after the deposition of Au SA. This suggests that most of the Au atoms were deposited within the NDC matrix and are rich in N-doped sites, which serve as anchor points for stabilizing the metal atoms. Figure 3d presents a HAADF-STEM image of an area containing Pt–Ni alloy NPs, with bright scattering dots (highlighted by numerous red circles) indicating the presence of scattered Au metallic species on the carbon support, likely existing as single atom sites. Figure 3e displays the STEM image of the area with only individual Au atoms without the presence of Pt–Ni alloy NPs. 3D map intensity profile of the selected atoms marked with an orange box in (e) identified the well-isolated Au SA with distinct higher intensity (as shown in Figure 3f). The STEM-EDX element mappings of Pt, Ni, and Au are shown in Figures 3g and S11 (Supporting Information) further substantiates the presence of Pt, Ni, and Au elements in the $PtNi_{NPs}/Au_{SA}$-NDC hybrid catalyst. Therefore, the obtained highly crystalline octahedral Pt–Ni alloy NPs are closely surrounded by Au SAs within the NDC, which enhances activity and exposes active sites during electrochemical reactions, resulting in excellent catalytic performance.

In order to gain deeper insights into the mechanism affecting the electrochemical performance, the surface chemical composition of the as-prepared samples and the valence state of the constituent elements were investigated by XPS. The full survey spectrums also confirmed the presence of Pt, Ni, Au, N, and C in the as-prepared samples (**Figure 4a**). The elemental distribution on the surface of $PtNi_{NPs}/Au_{SA}$-NDC was determined to be 1.25 at.% of Pt, 0.74 at.% of Ni, 0.04 at.% of Au, and 6.64 at.% of N (as detailed in Table S1, Supporting Information). The analysis of the Au 4f spectrum in Figure 4b confirms the existence of Au SA species. This is evident from the two peaks with the binding energies of 83.78 and 87.61 eV, corresponding to the orbital energies of Au $4f_{7/2}$ and Au $4f_{5/2}$, respectively.[47] It can be split into $Au^{\delta+}$ (83.83 and 87.59 eV) and Au^0 (83.44 and 87.18 eV). The fitting results reveal that the area of $Au^{\delta+}$ peaks is significantly larger than that of Au^0, indicating the dominant existence of Au species as an Au SA,[47] which is consistent with HAADF-STEM observation in Figure 3d,e. Furthermore, when compared to the XPS spectrum of Au 4f in Au_{SA}-NDC material (Figure S12, Supporting Information), the $PtNi_{NPs}/Au_{SA}$-NDC exhibits a slightly positive shift in the $Au^{\delta+}$ peaks (Table S2, Supporting Information). These results reflect a robust interaction between Au and Pt–Ni alloy NPs, where the electrons may transfer from Au SAs to Pt–Ni alloy NPs.[17] The minor Zn 3p peaks are attributed to the presence of the residue of Zn from ZIF-8.

The high-resolution N 1s of $PtNi_{NPs}/Au_{SA}$-NDC and $PtNi_{NPs}$/NDC (Figure 4c–e) were deconvoluted into four distinct peaks centered at 398.0, 400.5, 399.6, and 402.7 eV. In accordance with previous reports, these deconvoluted peaks can be attributed to specific nitrogen species: pyridinic-N, graphitic-N, pyrrolic-N, and oxidized-N, respectively.[48] In particular, when comparing $PtNi_{NPs}/Au_{SA}$-NDC with $PtNi_{NPs}$/NDC, the N 1s spectrum of $PtNi_{NPs}/Au_{SA}$-NDC located at 398.96 (9.64%) exhibited a metal-N interaction, which can be indexed to Au-N_x species. Additionally, the high proportion of pyridinic-N in $PtNi_{NPs}/Au_{SA}$-NDC (34.64%) is generally expected to play a crucial role in capturing Au atoms and stabilizing them within the carbon matrix.[49,50] On the other hand, the presence of graphitic-N signifies a high degree of graphitization in the carbon support, corroborated by the Raman spectra (Figure S8, Supporting Information). As shown in Figure 4f and Table S3 (Supporting Information), the high-resolution XPS spectrum of Pt 4f of $PtNi_{NPs}/Au_{SA}$-NDC can be deconvoluted into six peaks: metallic Pt^{2+} (located at 72.00 and 75.66 eV, 32.10%), Pt^0 (located at 71.06 and 74.44 eV, 57.70%) and minor Pt^{4+} (located at 73.28 and 77.44 eV, 10.19%).[51] The fitting results imply that the area of the peak corresponding to Pt^0 is much larger than that of Pt^{2+} and Pt^{4+}, indicating that the most active metallic Pt^0 exists on the surface of the hybrid catalyst. When comparing to Pt 4f in $PtNi_{NPs/}$NDC without Au SA sample (Figure 4g), the binding energy of Pt^0 in $PtNi_{NPs/}Au_{SA}$-NDC is shifted negatively by ≈0.3 eV. This shift reflects a higher electron density, likely due to the electron partial transfer from Au SAs to Pt–Ni alloy NPs. This electron transfer is also supported by the positive shift of the $Au^{\delta+}$ peak of $PtNi_{NPs}/Au_{SA}$-NDC compared to Au_{SA}-NDC, as mentioned previously. Importantly, this change in the Pt electronic structure can lead to a reduction in the binding energy of reactive intermediates, potentially enhancing the ORR performance.[52] The binding energies of Ni 2p peaks for $PtNi_{NPs}/Au_{SA}$-NDC (Figure 4h) indicate the coexistence of Ni^{2+} (located at 854.95 and 873.22 eV, 32.11%) and Ni^0 (located at 852.25 and 869.67 eV, 14.83%). In contrast, Ni 2p in $PtNi_{NPs}$/NDC (Figure 4i; Table S4, Supporting Information) exhibits higher binding energies and a lower proportion of Ni^0 peaks, further confirming that Au SAs implanted in the matrix of carbon support can donate electrons to Pt–Ni alloy NPs.

2.2. Oxygen Reduction Reaction Activity

To access the catalytic performance of the as-synthesized $PtNi_{NPs}/Au_{SA}$-NDC hybrid catalysts, ORR tests were performed. The linear sweep voltammetry shown in **Figure 5a** reveals that the half-wave potential ($E_{1/2}$) is 0.92 V versus the reversible hydrogen electrode (RHE) in 0.1 M $HClO_4$ solution. This performance surpasses $PtNi_{NPs}$/NDC without Au SA (0.84 V) and commercial 20 wt.% Pt/C (0.79 V). Moreover, the prepared Au_{SA}-NDC catalyst exhibits much lower activity ($E_{1/2}$ = 0.65), which is nearly equivalent to the blank NDC. To gain deeper insight into the ORR electrolysis of $PtNi_{NPs}/Au_{SA}$-NDC hybrid catalyst, the cycle voltammetry (CV) was collected in N_2- and O_2-saturated 0.1 M $HClO_4$ (Figure S13, Supporting Information). Compared to commercial Pt/C, the CV of $PtNi_{NPs}/Au_{SA}$-NDC hybrid catalyst displays a O_2 reduction peak at ≈0.9 V versus RHE, indicating superior ORR performance. This is further confirmed by the Tafel slope values in Figure 5b, which follow this order: $PtNi_{NPs}/Au_{SA}$-NDC (≈58.8 mV dec^{-1}) < $PtNi_{NPs}$/NDC (≈69.6 mV dec^{-1}) < Pt/C (≈78.5 mV dec^{-1}) < Au_{SA}-NDC (≈225.2 mV dec^{-1}) < NDC

© 2024 The Authors. Small published by Wiley-VCH GmbH

16136829, 2024, 34, Downloaded from https://onlinelibrary.wiley.com/doi/10.1002/smll.202311971 by Jeonbuk National University, Wiley Online Library on [18/10/2026]. See the Terms and Conditions (https://onlinelibrary.wiley.com/terms-and-conditions) on Wiley Online Library for rules of use; OA articles are governed by the applicable Creative Commons License

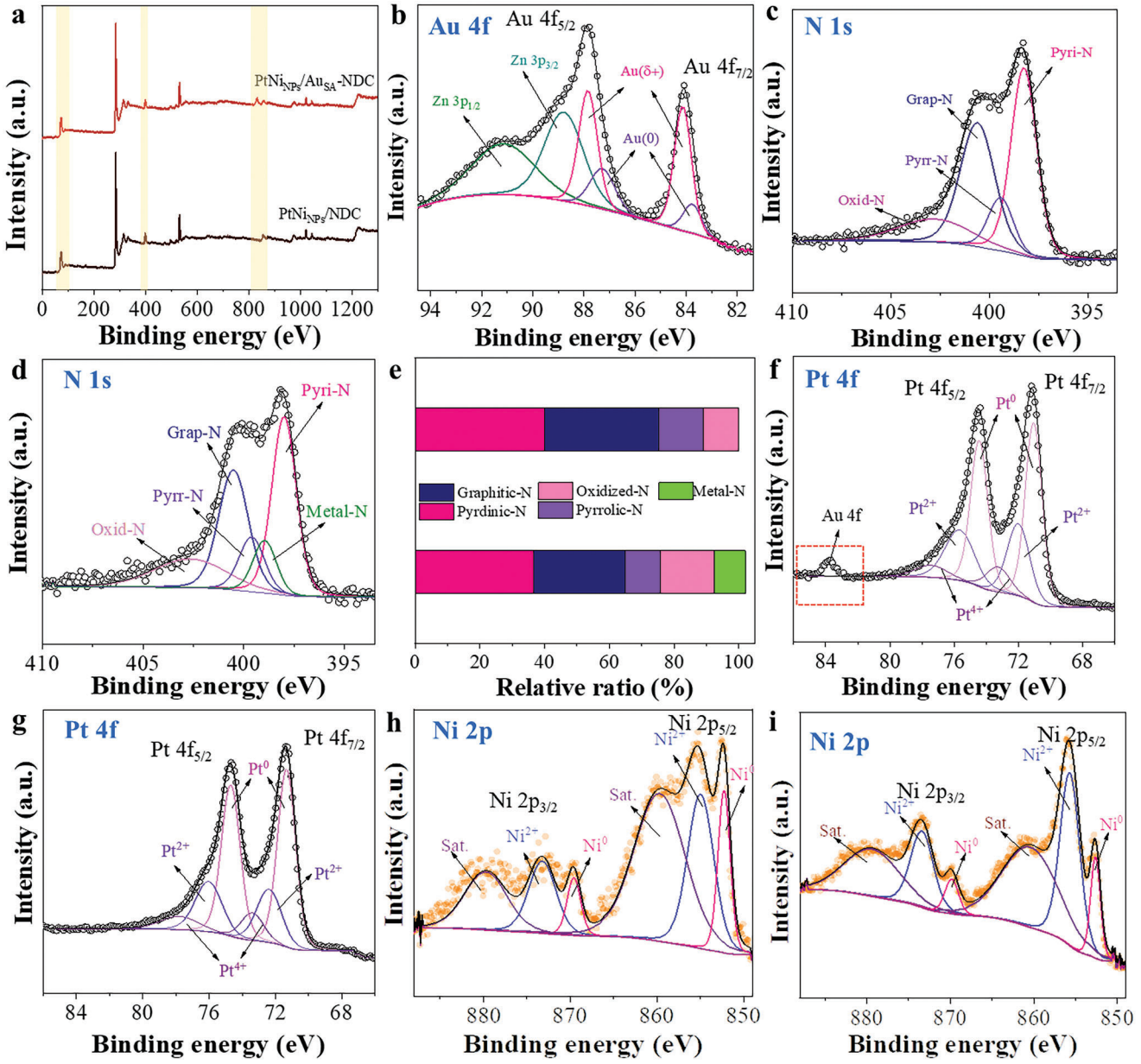


Figure 4. a) Full survey XPS spectra of PtNi$_{NPs}$/Au$_{SA}$-NDC and PtNi$_{NPs}$/NDC. b) High-resolution XPS spectra of Au 4f in PtNi$_{NPs}$/Au$_{SA}$-NDC. High-resolution XPS spectra of N 1s in c) PtNi$_{NPs}$/Au$_{SA}$-NDC, d) PtNi$_{NPs}$/NDC, and e) the relative ratio of different nitrogen species. High-resolution XPS spectra of Pt 4f in f) PtNi$_{NPs}$/Au$_{SA}$-NDC and g) PtNi$_{NPs}$/NDC. High-resolution XPS spectra of Ni 2p in h) PtNi$_{NPs}$/Au$_{SA}$-NDC and i) PtNi$_{NPs}$/NDC.

(≈268.7 mV dec^{-1}). These results signify faster ORR kinetics on PtNi$_{NPs}$/Au$_{SA}$-NDC. To evaluate the enhancement in Pt utilization of the catalyst, their mass activity at 0.9 V (vs RHE) is shown in Figure 5c. PtNi$_{NPs}$/Au$_{SA}$-NDC exhibits superior mass activity of 0.94 A mg$^{-1}{}_{Pt}$ at 0.9 V, which is 20.4 and 4.7 times higher than that of Pt/C (0.046 A mg$^{-1}{}_{Pt}$) and PtNi$_{NPs}$/NDC (0.20 A mg$^{-1}{}_{Pt}$), respectively. The catalytic selectivity of PtNi$_{NPs}$/Au$_{SA}$-NDC hybrid catalyst was determined by the Koutecky–Levich equation based on the ORR polarization curves over a range of rotation rates from 600 to 2000 rpm (Figure 5d; Figure S14, Supporting Information) with a scan rate of 10 mV s^{-1}. The electron transfer number (n) value is estimated to be 3.96 at the potential range from 0.8–0.9 V versus RHE, suggesting that this hybrid catalyst could rapidly reduce oxygen into water via a direct four-electron pathway ($O_2 + 4H^+ + 4e^- \rightarrow 2H_2O$).

The observed excellent activity suggests a strong interaction between Pt–Ni alloy NPs and Au SAs. To identify the synergistic effect, poisoning experiments were carried out using ethylenediaminetetraacetic acid disodium (EDTA-2Na) and potassium thiocyanide (KSCN).[8,53,54] As seen in Figure S15a (Supporting Information), after adding 10 mM EDTA-2Na to the electrolyte, the half-wave potential of PtNi$_{NPs}$/Au$_{SA}$-NDC significantly decreased. Conversely, ORR polarization of PtNi$_{NPs}$/NDC remained relatively stable after adding EDTA-2Na (Figure S15b, Supporting

© 2024 The Authors. Small published by Wiley-VCH GmbH

16136829, 2024, 34, Downloaded from https://onlinelibrary.wiley.com/doi/10.1002/smll.202311971 by Jeonbuk National University, Wiley Online Library on [18/10/2026]. See the Terms and Conditions (https://onlinelibrary.wiley.com/terms-and-conditions) on Wiley Online Library for rules of use; OA articles are governed by the applicable Creative Commons License

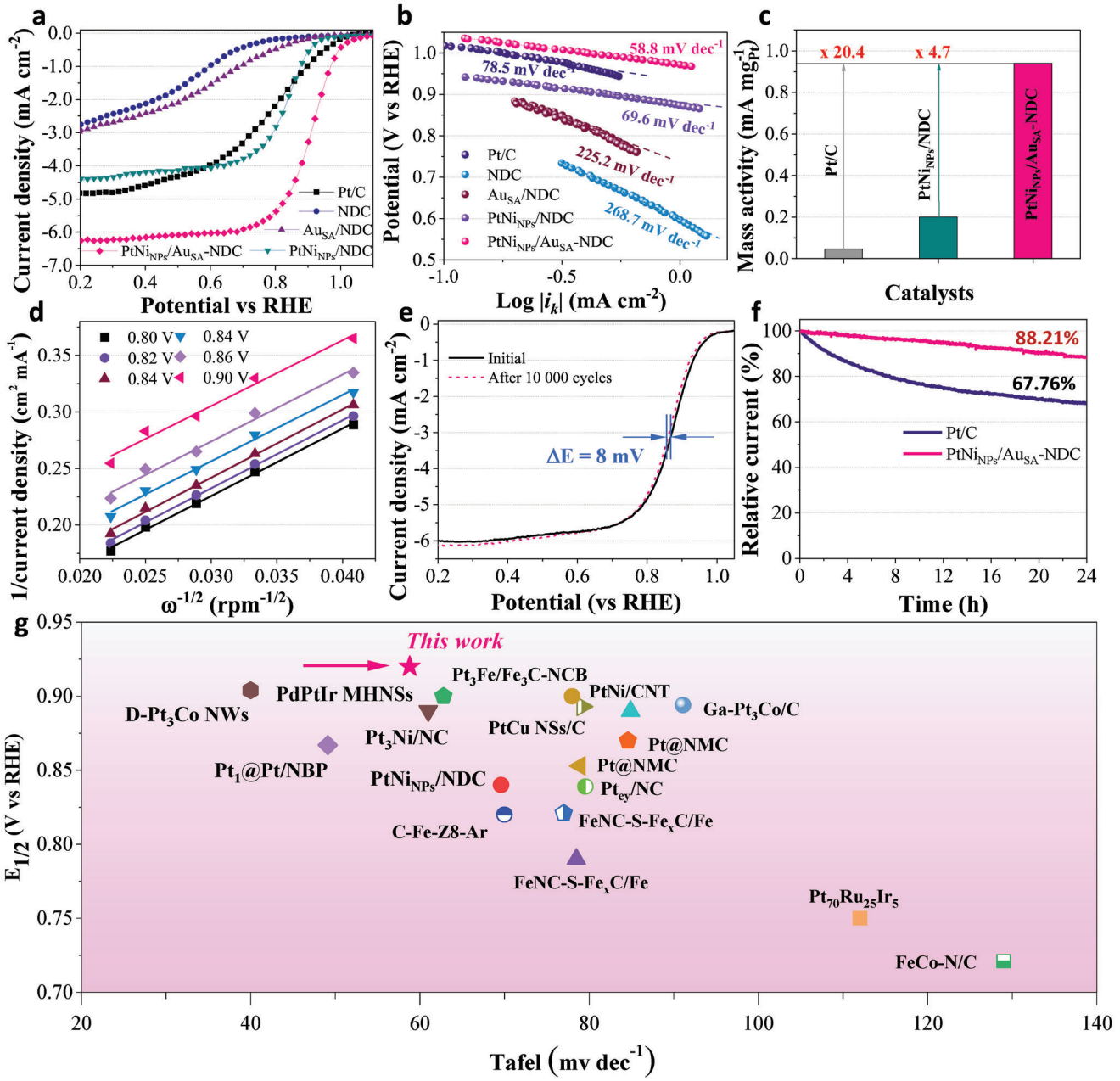


Figure 5. Electrochemical ORR performance of $PtNi_{NPs}/Au_{SA}$-NDC, $PtNi_{NPs}$/NDC, Au_{SA}-NDC, NDC, and commercial Pt/C. a) Linear sweep voltammetry (LSV) curves recorded in an O_2-saturated 0.1 M $HClO_4$ solution at a rotation speed of 1600 rpm and a scan rate of 5 mV s^{-1}. The corresponding b) Tafel plots and c) mass activity. d) Koutecky–Levich plots of $PtNi_{NPs}/Au_{SA}$-NDC collected from the ORR polarization curves. e) ORR polarization curves of $PtNi_{NPs}/Au_{SA}$-NDC before and after ADT and f) chronoamperometry stability of $PtNi_{NPs}/Au_{SA}$-NDC. g) Comparison of the Tafel slope and half-wave potential for various Pt-based or typical ORR catalysts in acidic electrolytes.

Information). These results imply the dominant role of Au SA for ORR. In contrast, the ORR activity of these materials dramatically diminished with the presence of 10 mM KSCN in the electrolyte. Considering that EDTA-2Na only poisons the SA active sites and KSCN affects both NPs and SA metals active sites, EDTA inhibits the activity of Au SA, while KSCN inactivates all metal sites.[55] The notable performance change observed in the EDTA-2Na and KSCN poisoning tests indicates contributions from both Au SA and Pt–Ni alloy NPs to ORR electrocatalysis.

In addition, the durability of $PtNi_{NPs}/Au_{SA}$-NDC was further investigated. The hybrid catalysts were subjected to continuous cycle voltammetry for 10 000 cycles between 0.6 and 1.0 V in an O_2-saturated 0.1 M $HClO_4$ electrolyte. The obtained $PtNi_{NPs}/Au_{SA}$-NDC exhibited excellent stability, with only an 8 mV $E_{1/2}$ loss, significantly smaller than that of Pt/C (≈90 mV) and $PtNi_{NPs}$/NDC (34 mV), as depicted in Figures 5f and S16 and S17 (Supporting Information). It is noteworthy to mention that the negligible loss in the $E_{1/2}$ of NDC is mainly due to the

© 2024 The Authors. Small published by Wiley-VCH GmbH

16136829, 2024, 34, Downloaded from https://onlinelibrary.wiley.com/doi/10.1002/smll.202311971 by Jeonbuk National University, Wiley Online Library on [18/10/2026]. See the Terms and Conditions (https://onlinelibrary.wiley.com/terms-and-conditions) on Wiley Online Library for rules of use; OA articles are governed by the applicable Creative Commons License

corrosion of carbon during the potential cycles.[56] This result is further supported by the chronoamperometry tests shown in Figure 5g, where the $PtNi_{NPs}/Au_{SA}$-NDC exhibits current retention as high as 88.21% after 24 h of operation, while the commercial Pt/C shows only 67.76% current retention. This result demonstrates that the as-prepared catalyst offers superior stability compared to state-of-the-art Pt/C. The improved stability can be attributed to the strong PtNi-Au_1-N_xC interaction in the $PtNi_{NPs}/Au_{SA}$-NDC hybrid catalyst during the ORR electrochemical process. The Au SA sites in N-rich doped carbon act as charge redistribution support, collaborating with Pt–Ni alloy NPs to establish a strong alloy NPs—support interaction. This strengthened interaction prevents Pt–Ni alloy NPs from migrating and aggregating during potential cycling, contributing to the excellent long-term durability of $PtNi_{NPs}/Au_{SA}$-NDC.

In order to study the commercial reliability of $PtNi_{NPs}/Au_{SA}$-NDC catalyst, the performance of MEAs utilizing different cathodes, such as Pt/C (120 μg_{Pt} cm^{-2}) and $PtNi_{NPs}/Au_{SA}$-NDC (33 μg_{Pt} cm^{-2}), in PEMFCs is presented in Figure S18 (Supporting Information). The $PtNi_{NPs}/Au_{SA}$-NDC MEA achieved a maximum power density of 0.77 W cm^{-2}, with an outstanding Pt utilization efficiency of 23.3 W mg_{Pt}^{-1}. In contrast, although the Pt/C MEA demonstrated a higher maximum power density of 0.83 W cm^{-2}, its Pt utilization efficiency was lower (23.3 W mg_{Pt}^{-1}). This difference could be attributed to the notably higher Pt loading in the Pt/C cathode compared to the $PtNi_{NPs}/Au_{SA}$-NDC MEA. Overall, the PEMFC performance indicates a significant enhancement of Pt utilization in this novel $PtNi_{NPs}/Au_{SA}$-NDC catalyst.

2.3. Hydrogen Evolution Reaction Activity

The hydrogen evolution reaction activity of $PtNi_{NPs}/Au_{SA}$-NDC and control samples were evaluated in 0.5 M H_2SO_4, and the results are shown in **Figure 6**. The iR-corrected LSV polarization curves of the synthesized samples are displayed in Figure 6a. The $PtNi_{NPs}/Au_{SA}$-NDC catalyst exhibits substantially higher geometric HER current density (J) compared to the $PtNi_{NPs}$/NDC material at the same overpotential, primarily due to the electronic modulation between Au SA and Pt–Ni alloy NPs. The as-prepared $PtNi_{NPs}/Au_{SA}$-NDC catalyst displayed an overpotential of 19.1 mV at a current density of 10 mA cm^{-2}, whereas the $PtNi_{NPs}$/NDC catalyst required an overpotential of 31.4 mV (Figure 6b) to achieve the same current density. Importantly, the HER activity of $PtNi_{NPs}/Au_{SA}$-NDC surpasses that of Pt/C commercial catalyst (with an overpotential of 47.9 mV at 10 mA cm^{-2}). In contrast, NDC showed virtually no catalytic activity for HER, indicating that the HER reaction occurs predominantly on the metal sites. To gain insights into the kinetics and mechanism of electrocatalysis, Tafel slopes were obtained by fitting the linear sections of Tafel plots.[57] As shown in Figure 6c, the Tafel slope of $PtNi_{NPs}/Au_{SA}$-NDC (21.0 mV dec^{-1}) is significantly lower than those of $PtNi_{NPs}$/NDC (42.6 mV dec^{-1}), Au_{SA}/NDC (275.5 mV dec^{-1}) and even than that of Pt/C (48.8 mV dec^{-1}). The favorable Tafel slope value of $PtNi_{NPs}/Au_{SA}$-NDC for HER kinetics suggests efficient hydrogen transfer pathways provided by the multiple porosity and adsorption of H^+ ions on the catalyst's surface. According to these results, the catalytic activity of $PtNi_{NPs}/Au_{SA}$-NDC for HER follows the Volmer–Tafel mechanism, where the Tafel step is the rate-determining step at low overpotentials.[1] Moreover, electrochemical impedance spectroscopic (EIS) experiments were conducted to deeply understand the catalytic kinetics of $PtNi_{NPs}/Au_{SA}$-NDC (Figure S19, Supporting Information). The charge-transfer resistance (R_{ct}) of $PtNi_{NPs}/Au_{SA}$-NDC is 3.12 Ω, while that for $PtNi_{NPs}$/NDC, Au_{SA}/NDC, NDC, and commercial Pt/C catalysts are 4.01, 28.06, 12.63 and 5.69 Ω, respectively. These results suggest that the fast electron transfer is facilitated on $PtNi_{NPs}/Au_{SA}$-NDC, supporting its intrinsic HER activity. From a practical perspective of water electrolysis, mass activity is a crucial parameter. Figure 6d shows that the $PtNi_{NPs}/Au_{SA}$-NDC exhibits an excellent mass activity of 12.4 and 41.5 mA cm^{-2} $mg^{-1}{}_{Pt}$, significantly higher than that of Pt/C (0.12 and 6.8 mA cm^{-2} $mg^{-1}{}_{Pt}$) and $PtNi_{NPs}$/NDC (5.5 and 17.1 mA cm^{-2} $mg^{-1}{}_{Pt}$) recorded at 25 and 50 mV, respectively. As shown in Figure S20 (Supporting Information), the introduction of 10 mM EDTA-2Na resulted in a negative shift of 78. mV in the η_{10} value of $PtNi_{In\ addition}$-NDC. Addition, the catalyst activity was completely deactivated with the addition of 10 mM KSCN. These observations are consistent with the results of the poisoning test in ORR activity, providing strong confirmation of the synergistic coupling effect between $PtNi_{NPs}$ and Au_{SA}, resulting in the enhancement in ORR and HER activity.

Besides activity, catalytic stability is an equally vital criterion in practical applications. Figure 6e displays the polarization curves of the $PtNi_{NPs}/Au_{SA}$-NDC catalyst before and after 10 000 cycles. The accelerated CV test provides insight into the robustness of $PtNi_{NPs}/Au_{SA}$-NDC in HER catalytic activity, showing virtually unchanged polarization curves and maintaining a low overpotential (ΔE = 6.9 mV) at 10 mA cm^{-2}. In contrast, the commercial Pt/C catalyst experiences significant degradation, exhibiting an approximate decrease of 14.9 mV in overpotential after 10 000 cycles (Figure 6f). These results comprehensively affirmed the commendable stability of as-prepared $PtNi_{NPs}/Au_{SA}$-NDC electrocatalysts. A comparison of the overpotential and Tafel slope is presented in Figure 6g. Evidently, the optimized $PtNi_{NPs}/Au_{SA}$-NDC catalyst demonstrates a significantly lower overpotential and enhanced HER kinetics, surpassing recent reports on Pt-based catalysts.

2.4. Density Functional Theory Analysis

To gain a comprehensive understanding of the original ORR and HER mechanisms, density functional theory (DFT) calculations were performed. Considering the results of our physical/electrochemical characterizations and computational feasibility, the $PtNi_{NPs}/Au_{SA}$-NDC model is composed of an N-doped graphene sheet embedded with an atomic Au site and a small decorated Pt–Ni alloy cluster (PtNi/Au-N_4). Figure S21 (Supporting Information) shows several slab models of Au SA on an N-doped graphene sheet, including Au-C_4, Au-N_1-C_3, Au-N_2-C_2, Au-N_3-C_1, and Au-N_4. The formation energies of these models were summarized in Table S5 (Supporting Information). Among these Au SA structures, the formation energy of the Au-N_4 site obtained from DFT calculations is −5.4 eV, the lowest value compared to other Au SA sites. This low negative of E_f suggests that the formation of Au-N_4 sites in Au SA is more favorable.

© 2024 The Authors. Small published by Wiley-VCH GmbH

16136829, 2024, 34, Downloaded from https://onlinelibrary.wiley.com/doi/10.1002/smll.202311971 by Jeonbuk National University, Wiley Online Library on [18/10/2026]. See the Terms and Conditions (https://onlinelibrary.wiley.com/terms-and-conditions) on Wiley Online Library for rules of use; OA articles are governed by the applicable Creative Commons License

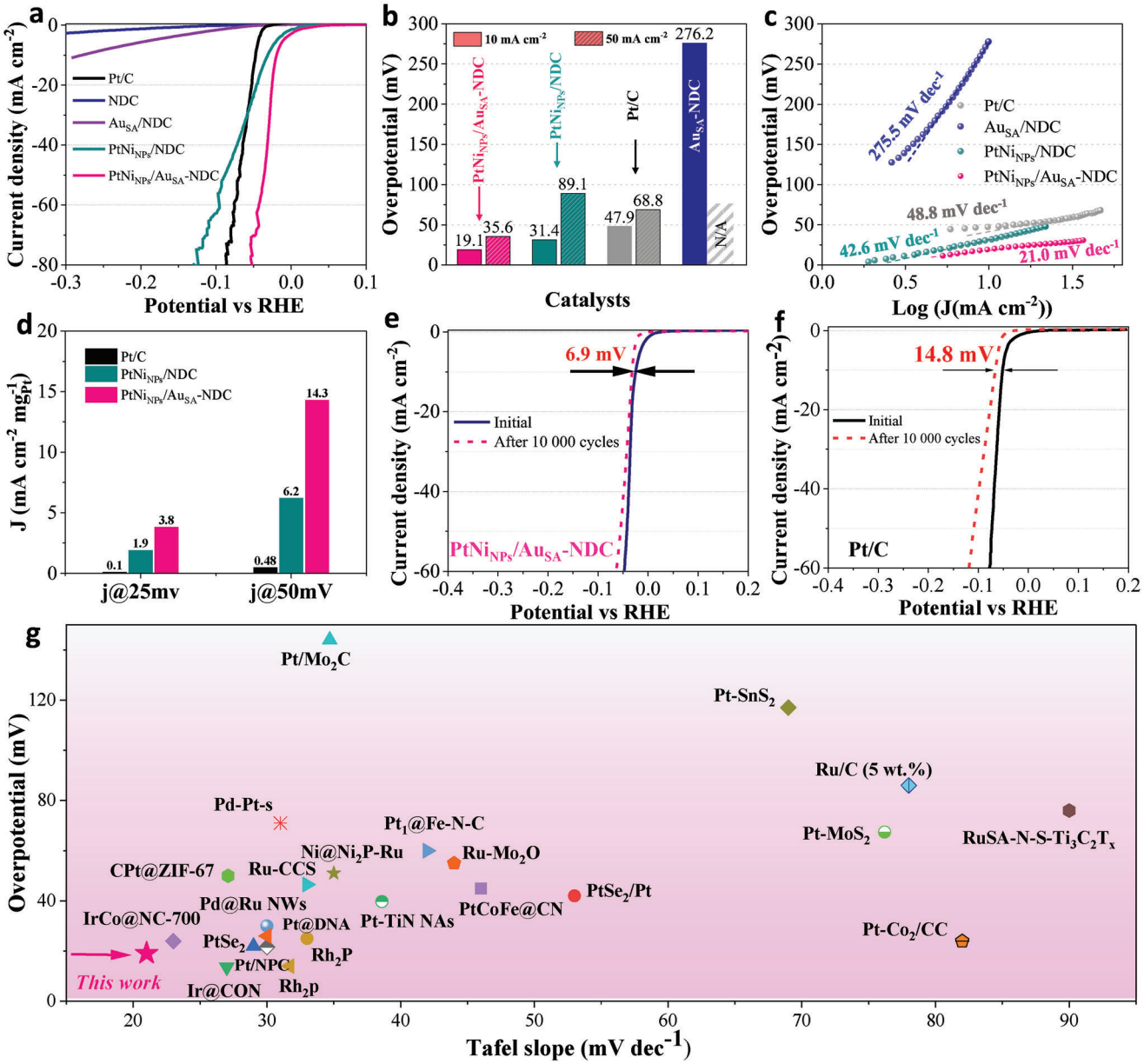


Figure 6. a) HER polarization curves of $PtNi_{NPs}/Au_{SA}$-NDC, $PtNi_{NPs}$/NDC, Au_{SA}/NDC, NDC, and 20 wt.% Pt/C in 0.5 M H_2SO_4 solution at a scan rate of 5mV s^{-1}, b) the corresponding overpotential of these catalyst materials @j=10/50 mA cm^{-2}, c) Tafel slopes of different catalyst materials, d) Mass activity of $PtNi_{NPs}/Au_{SA}$-NDC, $PtNi_{NPs}$/NDC and e) Pt/C at 25 and 50 mV, and f) LSV polarization curves of $PtNi_{NPs}/Au_{SA}$-NDC and Pt/C before and after 10 000 CV cycles, respectively. g) Comparison of the Tafel slope and overpotential for various Pt-based or typical HER catalysts in acidic electrolytes.

The optimized models Pt–Ni alloy cluster decorated N-doped graphene sheet (PtNi/NDC) were also created for comparison (**Figure** 7a–c). To examine the electronic structures modulation between Pt–Ni alloy sites and atomic Au sites, the computational partial density of state (PDOS) was further analyzed (Figure 7d). As depicted, the PtNi/Au-N_4 exhibits the highest density of states near the Fermi level compared to PtNi/NDC and Au-N_4. This suggests significantly enhanced electron transfer for $PtNi_{NPs}/Au_{SA}$-NDC hybrid catalyst, which possesses higher conductivity and catalytic performance. Furthermore, the d orbital (the primary orbitals that contributed to the enhanced DOS) in the PtNi/Au-N_4 is closer to the Fermi level than that of PtNi/NDC, indicating the presence of electron interaction between the Au-N_4 sites and Pt–Ni clusters. These results are in concordance with the experimental data and reveal stronger adsorption of ORR/HER reaction intermediates on $PtNi_{NPs}/Au_{SA}$-NDC than on $PtNi_{NPs}$/NDC, promoted by electrons transfer from Au sites to Pt–Ni alloy NPs.

According to the ORR free energy diagram in Figure 7e, the rate-determining step (RDS) of PtNi/Au-N_4 and PtNi/NDC is the generation step of *OH from *O (*O + H^+ +e^- → *OH). The corresponding free energy changes for ORR at 0.9 V are 3.59 for PtNi/Au-N_4 and 3.78 eV for PtNi/NDC. These values

© 2024 The Authors. Small published by Wiley-VCH GmbH

16136829, 2024, 34, Downloaded from https://onlinelibrary.wiley.com/doi/10.1002/smll.202311971 by Jeonbuk National University, Wiley Online Library on [18/10/2026]. See the Terms and Conditions (https://onlinelibrary.wiley.com/terms-and-conditions) on Wiley Online Library for rules of use; OA articles are governed by the applicable Creative Commons License

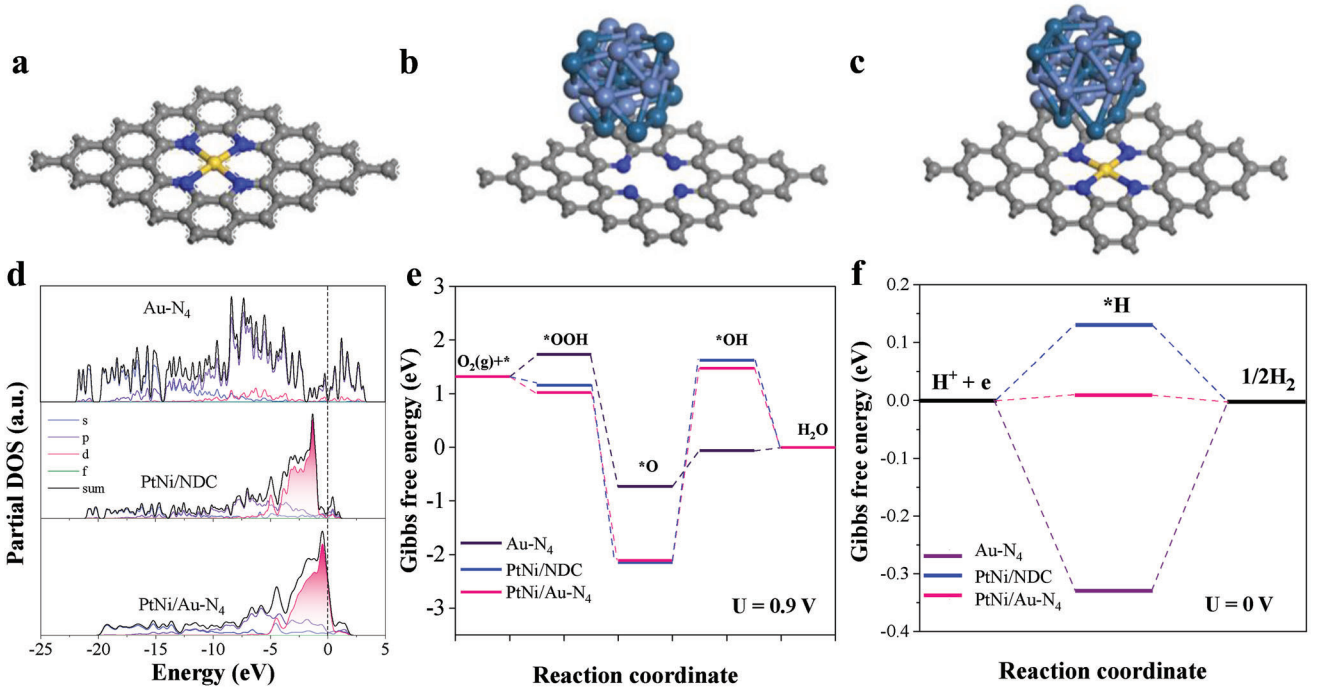


Figure 7. DFT calculations. The structural slab models in the DFT calculations: a) Au-N_4, b) Pt–Ni alloy, and c) Pt–Ni alloy cluster decorated on Au-N_4 nanosheet. Color code: Pt (dark blue), Ni (dark cyan), Au (yellow), C (gray), and N (blue). d) The calculated partial density of state (PDOS), the dark line denotes the position of the Fermi level. The Gibbs free energies diagrams for e) ORR and f) HER pathway correspond to these slab models.

indicate that PtNi/Au-N_4 exhibits higher activity in the four-electron ORR path than PtNi/NDC. Interestingly, the Au-N_4 sites are unfavorable for the entirely ORR process as they involve energy uphill steps during the formation of *OOH and *OH intermediates. However, the Au-N_4 site seems to favor the *OH generation process compared with PtNi/Au-N_4 and PtNi/NDC, requiring only 0.79 eV. This suggests that the neighboring heterogeneous Au-N_4 sites could accelerate the conversion of *O to *OH at the Pt–Ni cluster sites, collectively completing the four-electron transfer path. Consequently, the catalytic efficiency of the $PtNi_{NPs}/Au_{SA}$-NDC hybrid catalyst surpasses that of $PtNi_{NPs}$/NDC and Au_{SA}-NDC in ORR. Further details of the optimized adsorption structures for each ORR intermediate and their Gibbs free energy values can be found in Figures S22–S24 and Table. S6 (Supporting Information).

Regarding the HER process, it has been reported that catalysts with a Gibbs free energy of *H adsorption (ΔG_{*H}) close to zero exhibited highly efficient HER electrocatalysts.[58,59] The optimized *H adsorption structure and ΔG_{*H} values of different sites were calculated and shown in Figures 7f and S25 (Supporting Information), demonstrating a superior ΔG_{H*} for PtNi/Au-N_4 compared to that of PtNi/NDC and Au-N_4. The calculated ΔG_{*H} value for the PtNi/Au-N_4 is 0.01 (Table S7, Supporting Information), which is closer to 0 eV than that of PtNi/NDC and Au-N_4 (ΔG_{*H} = 0.13 and −0.33 eV, respectively). These results indicate that the presence of Au SA sites in $PtNi_{NPs}/Au_{SA}$-NDC effectively facilitates the adsorption of *H ($H^+ + e^- \rightarrow$ *H) in the HER process. The collective achievements in ORR/HER can be attributed to the presence of Au SA sites in $PtNi_{NPs}/Au_{SA}$-NDC, which generates a unique charge redistribution through electron transfer from Au sites to neighboring Pt–Ni alloy sites. As a result, the electronic structure of Pt–Ni alloy sites was optimized, leading to superior electrocatalytic behavior compared to other sites.

3. Conclusion

$PtNi_{NPs}/Au_{SA}$-NDC nanocomposites, in which Au SAs are tightly clamped between Pt–Ni alloy NPs and N-doped carbon, were successfully synthesized. The prepared hybrid structure catalyst exhibited sustained intrinsic activity in terms of mass activity found to be 0.94 A mg_{Pt}^{-1} at 0.9 V versus RHE and a negligible 8 mV potential decreased after 10 000 cycles test, establishing it as one of the top-performing ORR electrocatalysts. Additionally, the catalyst demonstrated superior HER performance with a low overpotential of 19.1 mV at 10 mA cm^{-2} and excellent long-term stability, experiencing only a potential drop of 6.9 mV after 10 000 cycles test. The remarkable electrocatalytic performance of $PtNi_{NPs}/Au_{SA}$-NDC was attributed to the synergistic effect between Pt–Ni alloy NPs and Au SA in NDC. Moreover, the XPS spectroscopy results implied the formation of a robust interaction between the alloy NPs and support, in which the Au SA in the NDC acts as an electron donor to the Pt–Ni alloy NPS site. This interaction effectively prevented Pt–Ni alloy NPs from migrating and aggregating during potential cycling, thus improving the durability of the catalyst. DFT simulation results further confirmed that the formation of the stable Au-N_4 site can effectively tailor the electronic structure of Pt–Ni alloy by elevating the energy level of d orbitals to near the Fermi level. As a result, this unique $PtNi_{NPs}$/Au-N_4 structure played a critical role in reducing the energy barrier of the *OH adsorption

© 2024 The Authors. Small published by Wiley-VCH GmbH

16136829, 2024, 34, Downloaded from https://onlinelibrary.wiley.com/doi/10.1002/smll.202311971 by Jeonbuk National University, Wiley Online Library on [18/10/2026]. See the Terms and Conditions (https://onlinelibrary.wiley.com/terms-and-conditions) on Wiley Online Library for rules of use; OA articles are governed by the applicable Creative Commons License

step (RDS step) in the ORR process and weakening the *H adsorption energy to promote the HER process. Our novel synthetic approach and intriguing findings not only enrich the array of Pt-based bifunctional ORR/HER electrocatalysts but also offer valuable insights for potential applications in fuel cells and beyond.

Supporting Information

Supporting Information is available from the Wiley Online Library or from the author.

Acknowledgements

This research was supported by the National Research Foundation (NRF) of Korea Grant funded by the Korean Government (MSIP) (NRF-2021R1A2C2008447), and the BK21-FOUR program of the MOE and NRF of Korea.

Conflict of Interest

The authors declare no conflict of interest.

Data Availability Statement

The data that support the findings of this study are available from the corresponding author upon reasonable request.

Keywords

electrocatalyst, hydrogen evolution reaction, oxygen reduction reaction, PtNi alloy NPs, single atoms

Received: December 20, 2023
Revised: March 17, 2024
Published online: May 10, 2024

[1] M. Wei, Y. Sun, F. Ai, S. Xi, J. Zhang, J. Wang, *Appl Catal B* **2023**, *334*, 122814.
[2] Y. Wang, D. F. Ruiz Diaz, K. S. Chen, Z. Wang, X. C. Adroher, *Mater. Today* **2020**, *32*, 178.
[3] Y. Lv, B. Kang, Y. Yuan, G. Chen, J. Y. Lee, *Chem. Eng. J.* **2022**, *430*, 133126.
[4] F. Cheng, J. Chen, *Chem. Soc. Rev.* **2012**, *41*, 2172.
[5] X. Ge, A. Sumboja, D. Wuu, T. An, B. Li, F. W. T. Goh, T. S. A. Hor, Y. Zong, Z. Liu, *ACS Catal.* **2015**, *5*, 4643.
[6] X. X. Wang, J. Sokolowski, H. Liu, G. Wu, *Chin. J. Catal.* **2020**, *41*, 739.
[7] Z. Ma, Z. P. Cano, A. Yu, Z. Chen, G. Jiang, X. Fu, L. Yang, T. Wu, Z. Bai, J. Lu, *Angew. Chem., Int. Ed.* **2020**, *59*, 18334.
[8] T. Duc Le, M. J. Ahemad, D.-S. Kim, B.-H. Lee, G.-J. Oh, G.-S. Shin, L. R. Nagappagari, V. Dao, T. Van Tran, Y.-T. Yu, *J. Colloid Interface Sci.* **2023**, *634*, 930.
[9] S. Y. Lim, S. Martin, G. Gao, Y. Dou, S. B. Simonsen, J. O. Jensen, Q. Li, K. Norrman, S. Jing, W. Zhang, *Adv. Funct. Mater.* **2021**, *31*, 2006771.
[10] Y. Xie, Y. Yang, D. A. Muller, H. D. Abruña, N. Dimitrov, J. Fang, *ACS Catal.* **2020**, *10*, 9967.
[11] X. Ye, Y. Xue, K. Li, W. Tang, X. Han, X. Zhang, Z. Song, Z. Zheng, Q. Kuang, *Mater. Adv.* **2021**, *2*, 5479.
[12] L. Gong, J. Liu, Y. Li, X. Wang, E. Luo, Z. Jin, J. Ge, C. Liu, W. Xing, *Chem. Eng. J.* **2022**, *428*, 131569.
[13] C. Cui, L. Gan, M. Heggen, S. Rudi, P. Strasser, *Nat. Mater.* **2013**, *12*, 765.
[14] V. Beermann, M. Gocyla, S. Kühl, E. Padgett, H. Schmies, M. Goerlin, N. Erini, M. Shviro, M. Heggen, R. E. Dunin-Borkowski, D. A. Muller, P. Strasser, *J. Am. Chem. Soc.* **2017**, *139*, 16536.
[15] L. Guo, W.-J. Jiang, Y. Zhang, J.-S. Hu, Z.-D. Wei, L.-J. Wan, *ACS Catal.* **2015**, *5*, 2903.
[16] J. Li, S. Sharma, X. Liu, Y.-T. Pan, J. S. Spendelow, M. Chi, Y. Jia, P. Zhang, D. A. Cullen, Z. Xi, H. Lin, Z. Yin, B. Shen, M. Muzzio, C. Yu, Y. S. Kim, A. A. Peterson, K. L. More, H. Zhu, S. Sun, *Joule* **2019**, *3*, 124.
[17] B. Liu, R. Feng, M. Busch, S. Wang, H. Wu, P. Liu, J. Gu, A. Bahadoran, D. Matsumura, T. Tsuji, D. Zhang, F. Song, Q. Liu, *ACS Nano* **2022**, *16*, 14121.
[18] Q. Feng, X. Wang, M. Klingenhof, M. Heggen, P. Strasser, *Angew. Chem., Int. Ed.* **2022**, *61*, e202203728.
[19] H. Zhai, G. Xu, J. Liu, T. Xu, C. Li, J. Bai, *Int. J. Hydrogen Energy* **2022**, *47*, 2423.
[20] Y.-G. Wang, D. Mei, V.-A. Glezakou, J. Li, R. Rousseau, *Nat. Commun.* **2015**, *6*, 6511.
[21] S. Cao, M. Yang, A. O. Elnabawy, A. Trimpalis, S. Li, C. Wang, F. Göltl, Z. Chen, J. Liu, J. Shan, M. Li, T. Haas, K. W. Chapman, S. Lee, L. F. Allard, M. Mavrikakis, M. Flytzani-Stephanopoulos, *Nat. Chem.* **2019**, *11*, 1098.
[22] M. Gao, D. Horita, Y. Ono, A. Lyalin, S. Maeda, T. Taketsugu, *J. Phys. Chem. C* **2017**, *121*, 2661.
[23] N. Siemer, D. Muñoz-Santiburcio, D. Marx, *ACS Catal.* **2020**, *10*, 8530.
[24] A. Matsuo, S. Hasegawa, S. Takano, T. Tsukuda, *Langmuir* **2020**, *36*, 7844.
[25] A. Lyalin, T. Taketsugu, *Faraday Discuss.* **2011**, *152*, 185.
[26] M. Gao, A. Lyalin, S. Maeda, T. Taketsugu, *J. Chem. Theory Comput.* **2014**, *10*, 1623.
[27] D. Eguchi, M. Sakamoto, T. Teranishi, *Chem. Sci.* **2018**, *9*, 261.
[28] X.-F. Yang, A. Wang, B. Qiao, J. Li, J. Liu, T. Zhang, *Acc. Chem. Res.* **2013**, *46*, 1740.
[29] Y. Shi, Z.-R. Ma, Y.-Y. Xiao, Y.-C. Yin, W.-M. Huang, Z.-C. Huang, Y.-Z. Zheng, F.-Y. Mu, R. Huang, G.-Y. Shi, Y.-Y. Sun, X.-H. Xia, W. Chen, *Nat. Commun.* **2021**, *12*, 3021.
[30] F. Xiao, Q. Wang, G.-L. Xu, X. Qin, I. Hwang, C.-J. Sun, M. Liu, W. Hua, H. Wu, S. Zhu, J.-C. Li, J.-G. Wang, Y. Zhu, D. Wu, Z. Wei, M. Gu, K. Amine, M. Shao, *Nat. Catal.* **2022**, *5*, 503.
[31] Z. Qiao, C. Wang, C. Li, Y. Zeng, S. Hwang, B. Li, S. Karakalos, J. Park, A. J. Kropf, E. C. Wegener, Q. Gong, H. Xu, G. Wang, D. J. Myers, J. Xie, J. S. Spendelow, G. Wu, *Energy Environ. Sci.* **2021**, *14*, 4948.
[32] W. Wu, Z. Zhang, Z. Lei, X. Wang, Y. Tan, N. Cheng, X. Sun, *ACS Appl. Mater. Interfaces* **2020**, *12*, 10359.
[33] L. Chong, J. Wen, J. Kubal, F. G. Sen, J. Zou, J. Greeley, M. Chan, H. Barkholtz, W. Ding, D.-J. Liu, *Science* **2018**, *362*, 1276.
[34] X. Ao, W. Zhang, B. Zhao, Y. Ding, G. Nam, L. Soule, A. Abdelhafiz, C. Wang, M. Liu, *Energy Environ. Sci.* **2020**, *13*, 3032.
[35] H. Wei, X. Liu, A. Wang, L. Zhang, B. Qiao, X. Yang, Y. Huang, S. Miao, J. Liu, T. Zhang, *Nat. Commun.* **2014**, *5*, 5634.
[36] J. Chen, H. Li, C. Fan, Q. Meng, Y. Tang, X. Qiu, G. Fu, T. Ma, *Adv. Mater.* **2020**, *32*, 2003134.
[37] N. Cheng, S. Stambula, D. Wang, M. N. Banis, J. Liu, A. Riese, B. Xiao, R. Li, T. K. Sham, L. M. Liu, G. A. Botton, X. Sun, *Nat. Commun.* **2016**, *7*, 13638.

© 2024 The Authors. Small published by Wiley-VCH GmbH

16136829, 2024, 34, Downloaded from https://onlinelibrary.wiley.com/doi/10.1002/smll.202311971 by Jeonbuk National University, Wiley Online Library on [18/10/2026]. See the Terms and Conditions (https://onlinelibrary.wiley.com/terms-and-conditions) on Wiley Online Library for rules of use; OA articles are governed by the applicable Creative Commons License

[38] T. R. Shojaei, M. A. M. Salleh, M. Tabatabaei, H. Mobli, M. Aghbashlo, S. A. Rashid, T. Tan, in *Synthesis, Technology and Applications of Carbon Nanomaterials*, (Eds: S. A. Rashid, R. N. I. Raja Othman, M. Z. Hussein), Elsevier, Amsterdam, **2019**, Ch. 11, pp. 247–277.
[39] T. Li, J. Liu, Y. Song, F. Wang, *ACS Catal.* **2018**, *8*, 8450.
[40] P. Huang, J. Huang, S. A. Pantovich, A. D. Carl, T. G. Fenton, C. A. Caputo, R. L. Grimm, A. I. Frenkel, G. Li, *J. Am. Chem. Soc.* **2018**, *140*, 16042.
[41] T. Hou, N. Luo, H. Li, M. Heggen, J. Lu, Y. Wang, F. Wang, *ACS Catal.* **2017**, *7*, 3850.
[42] H. Wei, K. Huang, D. Wang, R. Zhang, B. Ge, J. Ma, B. Wen, S. Zhang, Q. Li, M. Lei, C. Zhang, J. Irawan, L.-M. Liu, H. Wu, *Nat. Commun.* **2017**, *8*, 1490.
[43] V. Mohan, E. Wu, J. Heo, A. Das, P. K. Jain, *ACS Energy Lett.* **2021**, *6*, 1980.
[44] N. N. Kariuki, W. J. Khudhayer, T. Karabacak, D. J. Myers, *ACS Catal.* **2013**, *3*, 3123.
[45] Z. Hu, C. Yang, K. Lv, X. Li, Q. Li, J. Fan, *Chem. Commun.* **2020**, *56*, 1745.
[46] A. Das, S. Pisana, B. Chakraborty, S. Piscanec, S. K. Saha, U. V Waghmare, K. S. Novoselov, H. R. Krishnamurthy, A. K. Geim, A. C. Ferrari, A. K. Sood, *Nat. Nanotechnol.* **2008**, *3*, 210.
[47] C. Zhang, L. Fu, N. Liu, M. Liu, Y. Wang, Z. Liu, *Adv. Mater.* **2011**, *23*, 1020.
[48] Z. Duan, G. Henkelman, *J. Phys. Chem. C* **2020**, *124*, 12016.
[49] R. Lin, D. Albani, E. Fako, S. K. Kaiser, O. V Safonova, N. López, J. Pérez-Ramírez, *Angew. Chem., Int. Ed.* **2019**, *58*, 504.
[50] X. Han, X. Ling, D. Yu, D. Xie, L. Li, S. Peng, C. Zhong, N. Zhao, Y. Deng, W. Hu, *Adv. Mater.* **2019**, *31*, 1905622.
[51] X. Wang, Q. Zhang, H. Jiang, Y. Li, H. Zhu, L. Zheng, L. Gu, H.-P. Liang, *ACS Sustain. Chem. Eng.* **2023**, *11*, 10051.
[52] X.-F. Zhang, A.-J. Wang, L. Zhang, J. Yuan, Z. Li, J.-J. Feng, *ACS Appl. Energy Mater.* **2018**, *1*, 5054.
[53] C. Shi, Y. Liu, R. Qi, J. Li, J. Zhu, R. Yu, S. Li, X. Hong, J. Wu, S. Xi, L. Zhou, L. Mai, *Nano Energy* **2021**, *87*, 106153.
[54] P. Su, W. Pei, X. Wang, Y. Ma, Q. Jiang, J. Liang, S. Zhou, J. Zhao, J. Liu, G. Q. (Max) Lu, *Angew. Chem., Int. Ed.* **2021**, *60*, 16044.
[55] H. Chen, R. Ding, B.-W. Liu, F.-R. Zeng, H.-B. Zhao, *Small* **2023**, 2306274.
[56] L. Huang, Y.-Q. Su, R. Qi, D. Dang, Y. Qin, S. Xi, S. Zaman, B. You, S. Ding, B. Y. Xia, *Angew. Chem., Int. Ed.* **2021**, *60*, 25530.
[57] Z. Wang, K. Chi, S. Yang, J. Xiao, F. Xiao, X. Zhao, S. Wang, *Small* **2023**, *19*, 2301403.
[58] X. Liu, J. He, S. Zhao, Y. Liu, Z. Zhao, J. Luo, G. Hu, X. Sun, Y. Ding, *Nat. Commun.* **2018**, *9*, 4365.
[59] H.-J. Qiu, Y. Ito, W. Cong, Y. Tan, P. Liu, A. Hirata, T. Fujita, Z. Tang, M. Chen, *Angew. Chem., Int. Ed.* **2015**, *54*, 14031.

© 2024 The Authors. Small published by Wiley-VCH GmbH

16136829, 2024, 34, Downloaded from https://onlinelibrary.wiley.com/doi/10.1002/smll.202311971 by Jeonbuk National University, Wiley Online Library on [18/10/2026]. See the Terms and Conditions (https://onlinelibrary.wiley.com/terms-and-conditions) on Wiley Online Library for rules of use; OA articles are governed by the applicable Creative Commons License